PAPER

3D two-temperature magnetohydrodynamic modeling of fast thermal quenches due to injected impurities in tokamaks

View the article online for updates and enhancements.

3D two-temperature magnetohydrodynamic modeling of fast thermal quenches due to injected impurities in tokamaks

N.M. Ferraro[1], B.C. Lyons[2], C.C. Kim[3], Y.Q. Liu[2] and S.C. Jardin[1]

[1] Princeton Plasma Physics Laboratory, Princeton, NJ, United States of America
[2] General Atomics, San Diego, CA, United States of America
[3] SLS2 Consulting, San Diego, CA, United States of America

E-mail: nferraro@pppl.gov

Abstract

An integrated model for the ionization, radiation, and advection of impurities in the extended-magnetohydrodynamic code M3D-C1 is described. This implementation makes use of the KPRAD model, which calculates bremsstrahlung radiation and impurity ionization, recombination, and radiation rates using a model in which the density of each charge state is advanced separately. The integrated model presented here allows the independent evolution of electron and ion temperatures, which is necessary to accurately model cases where the electron temperature drops more quickly than the electron–ion thermal equilibration time. This model is used to simulate the disruption of a model NSTX discharge caused by the introduction of argon impurities, using physically realistic resistivity. Despite well-mixed impurities, contraction of the current channel is found to lead to magnetohydrodynamic instabilities that result in stochastization of the magnetic field, a fast thermal quench, and localized parallel electric fields that can exceed the axisymmetric values by a factor of five for brief periods.

Keywords: tokamaks, disruptions, disruption mitigation

(Some figures may appear in colour only in the online journal)

1. Introduction

Disruption mitigation, the intentional cooling of the plasma to dissipate plasma current and thermal energy during a disruption, is critical for ensuring the lifespan of plasma facing components on large fusion experiments such as ITER [1]. The primary method for disruption mitigation on present tokamaks is the injection of large quantities of cold ions through gas jets or pellets [2]. Considerable uncertainty still exists on the optimal type of gas to deliver, and on the method for delivering it, whether for the purpose of dissipating heat and current or suppressing runaway electrons. Methods such as shell pellets [3] and shattered pellets [4, 5] are presently favored for their ability to deliver gas relatively deep into the core of large devices such as ITER. Cooling the core, in particular, may have the advantage of avoiding the triggering of MHD instabilities that would result from contraction of the current channel. These instabilities can potentially result in non-axisymmetric forces on the tokamak, as well as a fast current quench that produces dangerous runaway electrons [6]. Therefore, quantitatively predicting the effectiveness of disruption mitigation methods on ITER, and optimizing those methods on present devices, requires an integrated model of the cooling from injected gas and the MHD instabilities that develop as a consequence.

The simulation of the pre-thermal-quench (pre-TQ) phase of disruption mitigation scenarios, in which the edge of the plasma cools due to impurity injection, can be simulated with one-dimensional [7] or two-dimensional (2D) [8] transport codes. How this phase affects the current density, which then has implications for the eventual breakup of magnetic surfaces and fast TQ, requires a 2D [9] and eventually fully

three-dimensional (3D) MHD treatment. Axisymmetric simulations of disruption mitigation in ITER that self-consistently include the effects of impurity radiation and current density evolution have been done using the axisymmetric TSC code [10]. Considerable work on the integration of impurity models in 3D (extended-MHD) simulations has been carried out by Izzo *et al* [11] using the KPRAD [12] impurity model and the NIMROD extended-MHD code. Notably, this model has yielded important insight on radiation asymmetry and the role of MHD activity in impurity transport in disruption mitigation experiments [13, 14]. Additionally, this work found that impurity injection plays an important role in triggering and setting the phase of MHD instabilities that lead to stochastization of the magnetic field, in some cases initiating a fast thermal quench. Similar results have also recently been found in JOREK simulations of disruption mitigation using deuterium injection in JET [15, 16]. More recently, NIMROD calculations have shown the effect of preexisting islands on impurity injection [17], as is expected to be the case when mitigating disruptions due to locked modes.

In extended-MHD simulations of disruption mitigation, it is typical to use a single temperature equation together with the assumption that T_e/T_i is constant in time. This is the case for the model used by Izzo, for example [13], and also in JOREK. This choice is appropriate on timescales long compared to the ion–electron temperature equilibration time, which can vary from ~ 10 ms for in the pre-TQ phase to ~ 10 μs in the post-TQ phase. Since the TQ itself typically proceeds on a ~ 1 ms timescale, the $T_e/T_i = $ const. assumption may not be well justified during the TQ. In particular, cooling during the thermal quench, whether from radiation, dilution from impurity ionization, or parallel thermal transport along stochastic field lines, will dominantly affect the electrons, and therefor the assumption of constant T_i/T_e will generally over-predict T_e and under-predict T_i when these processes are fast compared to the τ_Δ (assuming the model conserves total energy).

In section 2, we present two-temperature models that account properly for the evolution of both total energy and electron energy independently, and that accurately describe the evolution of T_e, in the presence of an impurity species. We also describe the implementation of these models in M3D-C1 [18, 19], a 3D finite element code. This code has previously been used to explore resistive wall instabilities and vertical displacement events that lead to large electromagnetic forces on conducting structures in tokamaks during disruptions [19, 20]. The implementation of the single-temperature model is verified through a benchmark with the NIMROD code in section 4, in which a core-localized source of impurities is simulated. We compare the predictions of two-temperature models with single-temperature models using different assumptions for relating T_e and T_i.

We then present results of 3D M3D-C1 simulations of the disruption of an NSTX plasma, caused by the introduction of neutral argon, in section 4.2. These simulations, done using physically realistic resistivity, show a contraction of the current channel, development of strong parallel electric fields at the plasma surface and associated skin currents, and Alfvénic instability of these skin currents leading to rapid stochastization of the magnetic field and a fast thermal quench. The implications of these observations and relation to existing theory are discussed in section 5.

2. Model

Here we consider a single-fluid model, in the sense that all charged species (electrons, main ions, and ionized impurities) are assumed to have the same fluid velocity $\vec{v}$. This assumption is made here for convenience due to the numerical challenges introduced by two-fluid effects. It is known that two-fluid effects can play an important role in processes such as reconnection that occur in disruptions, but we leave the exploration of these effects as future work. The densities of the main ions (n_i) and of each individual charge state of the impurity species, $n_Z^{(j)}$ for $1 \leqslant j \leqslant Z$, are advanced using the continuity equations

$$\frac{\partial n_i}{\partial t} + \nabla \cdot (n_i \vec{v}) = \nabla \cdot (D \nabla n_i) + \sigma_i \qquad (1)$$

$$\frac{\partial n_Z^{(j)}}{\partial t} + \nabla \cdot (n_Z^{(j)} \vec{v}) = \nabla \cdot (D \nabla n_Z^{(j)}) + \sigma_Z^{(j)}. \qquad (2)$$

The electron density is defined to satisfy quasi-neutrality

$$n_e = Z_i n_i + \sum_{j=1}^{Z} j\, n_Z^{(j)}. \qquad (3)$$

The particle source density for each impurity charge state, $\sigma_Z^{(j)}$, is calculated using the KPRAD model [12]. The electron momentum equation defines the generalized Ohm's law

$$\vec{E} = \eta \vec{J} - \vec{v} \times \vec{B}. \qquad (4)$$

The neutral impurity particle density $n_Z^{(0)}$ is advanced using the calculated ionization and recombination rates, but is not advected or diffused. Here and throughout, we neglect the electron mass ($m_e = 0$). The sum of momentum equations for all charged particles is

$$\rho \left(\frac{\partial \vec{v}}{\partial t} + \vec{v} \cdot \nabla \vec{v} \right) = \vec{J} \times \vec{B} - \nabla p - \nabla \cdot \Pi - \varpi \vec{v} \qquad (5)$$

where

$$\rho = m_i n_i + \sum_{j=1}^{Z} m_Z n_Z^{(j)} \qquad (6)$$

$$\varpi = m_i \sigma_i + \sum_{j=1}^{Z} m_Z \sigma_Z^{(j)}. \qquad (7)$$

It is assumed that all ionized impurities have the same temperature as the main ion species, T_i. The final term in equation (5) represents the slowing of the fluid velocity to conserve momentum as new particles are added.

Several models for advancing the ion and electron temperatures, either together or independently, are implemented in

M3D-C1. Each of these models are built from the electron temperature equation:

$$n_{\mathrm{e}}\left[\frac{\partial T_{\mathrm{e}}}{\partial t} + \vec{v}\cdot\nabla T_{\mathrm{e}} + (\Gamma-1)T_{\mathrm{e}}\nabla\cdot\vec{v}\right] + \sigma_{\mathrm{e}}T_{\mathrm{e}}$$
$$= (\Gamma-1)\left[\eta J^2 - \nabla\cdot\vec{q}_{\mathrm{e}} + Q_{\mathrm{e}} - \Pi_{\mathrm{e}}:\nabla\vec{v}\right] \tag{8}$$

and the sum of the temperature equations for all ion species (i.e. main ions and all ionized impurities):

$$n_*\left[\frac{\partial T_{\mathrm{i}}}{\partial t} + \vec{v}\cdot\nabla T_{\mathrm{i}} + (\Gamma-1)T_{\mathrm{i}}\nabla\cdot\vec{v}\right] + \sigma_* T_{\mathrm{i}}$$
$$= (\Gamma-1)\left[-\nabla\cdot\vec{q}_* + Q_* - \Pi_*:\nabla\vec{v} + \frac{1}{2}\varpi v^2\right]. \tag{9}$$

Here, n_*, σ_*, Π_*, Q_*, and $\vec{q}_*$ are sum over all ion species of the particle densities, particle source densities, stresses, energy density sources, and energy density fluxes, respectively. The final term in equation (9) accounts for the net loss of kinetic energy caused by the slowing of the fluid velocity as new particles are added. Models implemented include a single total pressure equation in which $p_{\mathrm{e}}/p_{\mathrm{i}}$ is assumed fixed; a single total temperature equation in which $T_{\mathrm{e}}/T_{\mathrm{i}}$ is assumed fixed; a two-pressure equation in which the total pressure p and electron pressure p_{e} are evolved separately; and a two-temperature model in which the electron temperature T_{e} and ion temperature T_{i} are evolved independently using equations (8) and (9). Each of these models conserves total energy, in the sense that all sources and sinks are are due to physical processes that are included in the model. For reference, these models are documented in appendix.

The electron heat source density Q_{e} is the sum of the heating from radiation and ionization Q_{rad} (this is negative for power lost from the plasma) and the collisional transfer of energy from the ions to the electrons Q_Δ [21]. The radiated power is calculated using the KPRAD module, and is the sum of the bremsstrahlung, line radiation, and recombination losses. We note that KPRAD calculates both the kinetic energy and potential energy released as radiation during recombination, but we only include the kinetic contribution in Q_{e}, since the potential contribution does not subtract from the kinetic energy of the electron fluid.

The equipartition term is the sum of the energy transfer from all ion species to electrons:

$$Q_\Delta = 3m_{\mathrm{e}}n_{\mathrm{e}}(T_{\mathrm{i}} - T_{\mathrm{e}})\left(\frac{\nu_{\mathrm{ei}}}{m_{\mathrm{i}}} + \sum_{j=1}^{Z}\frac{\nu_{\mathrm{e}Z}^{(j)}}{m_Z}\right) \tag{10}$$

where the collision rate between electrons and ion species j is

$$\nu_{\mathrm{e}j} = \frac{4\sqrt{2\pi}e^4 Z_j^2 n_j \ln\Lambda}{3\sqrt{m_{\mathrm{e}}}T_{\mathrm{e}}^{3/2}}. \tag{11}$$

Therefore one can write

$$Q_\Delta = 3\mu\,\nu_{\mathrm{e}H}\,n_{\mathrm{e}}\,(T_{\mathrm{i}} - T_{\mathrm{e}}) \tag{12}$$

where

$$\mu = \frac{m_{\mathrm{e}}}{n_{\mathrm{e}}}\left(\frac{Z_{\mathrm{i}}^2 n_{\mathrm{i}}}{m_{\mathrm{i}}} + \sum_{j=1}^{Z}\frac{j^2 n_Z^{(j)}}{m_Z}\right) \tag{13}$$

and where $\nu_{\mathrm{e}H}$ is the collision frequency for a pure Hydrogen plasma ($Z_j = 1$, $m_j = m_p$, $n_j = n_{\mathrm{e}}$). Similarly, summing the collisional drag between the electrons and each ion species, the total resistivity can be written in terms of the collision frequency for a pure hydrogen plasma scaled by an 'effective Z' [22]:

$$\eta = \frac{m_{\mathrm{e}}\nu_{\mathrm{e}H}}{n_{\mathrm{e}}e^2}Z_{\mathrm{eff}} \tag{14}$$

$$Z_{\mathrm{eff}} = \frac{Z_{\mathrm{i}}^2 n_{\mathrm{i}} + \sum_{j=1}^{Z} j^2 n_Z^{(j)}}{n_{\mathrm{e}}}. \tag{15}$$

The heat flux densities are defined by

$$\vec{q}_{\mathrm{e}} = -\kappa^{\mathrm{e}}\nabla T_{\mathrm{e}} - \kappa_\parallel^{\mathrm{e}}\frac{\vec{B}\vec{B}}{B^2}\cdot\nabla T_{\mathrm{e}} \tag{16}$$

$$\vec{q}_{\mathrm{i}} = -\kappa^{\mathrm{i}}\nabla T_{\mathrm{i}} - \kappa_\parallel^{\mathrm{i}}\frac{\vec{B}\vec{B}}{B^2}\cdot\nabla T_{\mathrm{i}}. \tag{17}$$

In the following results we have assumed, for simplicity, that $\kappa^{\mathrm{i}} = \kappa^{\mathrm{e}}$ and $\kappa_\parallel^{\mathrm{i}} = \kappa_\parallel^{\mathrm{e}}$, and that both quantities are constant and uniform in the simulation domain.

3. Numerical implementation

The time step is divided into three parts. First, the impurity charge states are advanced by evolving the ionization and recombination processes, as described below. Second is the 'MHD advance', in which the main ion density, fluid velocity, electron temperature, and ion temperature are advanced using either an implicit or split semi-implicit method [23]. Third, the impurity charge states are advected using the fluid velocity calculated in the MHD advance.

The impurity advance is done by subcycling equations for the evolution of each charge state density. The KPRAD module is used to calculate ionization, recombination, and radiation rates as functions of the electron temperature and electron density. This information is used to integrate a master equation for each charge state through a time δt equal to the MHD time step. The energy lost over that time to radiation and ionization, δW_{rad}, and the change in the number of electrons δn_{e} due to ionization and recombination are also integrated. Then the heat loss rate, Q_{rad}, and the electron density source rate, σ_{e}, are calculated for use in the electron temperature equation in the MHD advance by using $Q_{\mathrm{rad}} = \delta W_{\mathrm{rad}}/\delta t$ and $\sigma_{\mathrm{e}} = \delta n_{\mathrm{e}}/\delta t$. This procedure is carried out independently at each spatial integration point of the Gaussian integration quadrature used within each mesh element (M3D-C1 typically uses 25 points within a 2D triangular element or 60 points within a 3D triangular prism element). In this way, the

charge state densities, electron source density, and heat source density are known at each quadrature point, and can be used in the weak form of the equations of the MHD advance. This is both more efficient and more accurate than integrating the weak form of the master equations using the finite element basis.

4. Results

4.1. Axisymmetric simulation of impurities from localized core source

To verify the accuracy of the implementation of the impurity model described here, a benchmark simulation was conducted using both M3D-C1 and NIMROD. The simulation was initialized using an equilibrium reconstruction of DIII-D discharge 137611 at $t = 1950$ ms. The main ion (deuterium) particle density was assumed uniform at 10^{20} m^{-3}. No impurities were present initially. A constant source of neutral argon with a Gaussian spatial distribution was included

$$\sigma_z^{(0)} = \nu \frac{R_0}{R} \exp\left[-\frac{(R - R_0)^2 + (Z - Z_0)^2}{2\delta^2} \right] \quad (18)$$

with $\delta = 0.25$ m and $\nu = 10^{23}$ m^{-3} s^{-1}. Axisymmetry was assumed. For this benchmark, we use a model in which a single temperature equation is advanced and $T_e/T_i = $ const is assumed (model #2 in appendix), since this is the model implemented in NIMROD.

Results of this benchmark are shown in figure 1. Very good agreement is found between the M3D-C1 and NIMROD simulations for the electron density, thermal energy, and radiated power loss. This indicates that the ionization, recombination, and radiation rates are in close agreement for both codes.

One small but noticeable difference is that M3D-C1 shows a steeper decline in the electron number towards the end of the simulation, when the thermal energy of the plasma has been almost entirely radiated away. This difference is primarily due to the fact that NIMROD sets a temperature floor below which the ionization/recombination model is not invoked, which is done to improve numerical stability. This temperature floor suppresses recombination in the cold plasma in the NIMROD simulation. It does not lead to a significant difference in the electron thermal energy, since the plasma is already cold by this point.

4.2. Simulations of disruption due to globally distributed impurities

Here we consider the effect of a uniform distribution of impurities in an NSTX plasma. The simulation is initialized with an equilibrium typical of an NSTX H-mode. This equilibrium is nearly double-null diverted, with plasma current $I_P = 600$ kA, magnetic axis $R_0 = 0.99$ m, and vacuum toroidal field at the magnetic axis $B_T = 0.38$ T. The current profile is peaked off axis, with the minimum value of the safety factor $q_{min} \approx 2.25$ occurring at normalized poloidal flux $\psi_n \approx 0.26$. The safety factor on axis and at $\psi_n = 0.95$ are initially $q_0 \approx 2.6$ and $q_{95} \approx 10$, respectively. The temperature
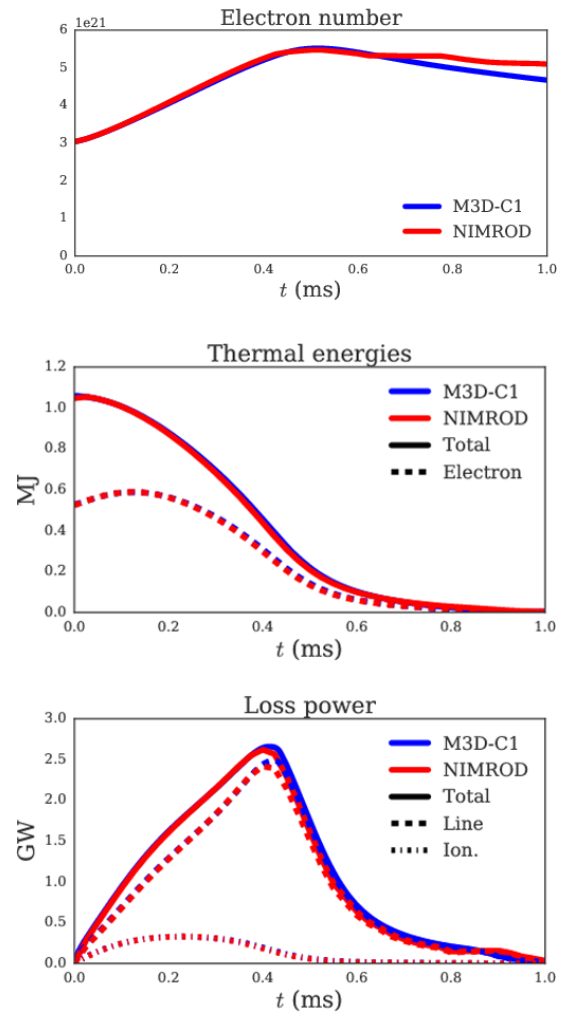

Figure 1. From the NIMROD / M3D-C1 benchmark, *top*: the total electron number in the simulation domain; *center*: the total thermal energy (solid line) and electron thermal energy (dashed line); and *bottom*: the total radiated power (solid line) with the separate contributions from line radiation (dashed line) and ionization (dotted line).

and density are initially peaked at $T_e = T_i \approx 2$ keV and $n_e = n_i \approx 1.9 \times 10^{19}$ on axis. The main ion species is deuterium. Here, the resistivity is determined by equation (14) without any artificial scaling factors. The Lundquist number at the magnetic axis is $S \approx 9 \times 10^7$. Anisotropic thermal conductivity is used with $\chi_\perp = \kappa_\perp/n_e \approx 8$ m^2 s^{-1} initially at the magnetic axis, and $\kappa_\parallel/\kappa_\perp = 10^6$ ($\kappa_\perp$ and $\kappa_\parallel$ are constant and uniform). A large viscosity is used for numerical stability, with $\nu_\perp = \mu_\perp/(m_i n_i) \approx 800$ m^2 s^{-1} initially at the magnetic axis ($\mu_\perp$ is constant and uniform). No external heating or current drive is included in these calculations due to the short timescales under consideration. In the absence of impurities, we find that the decay of the thermal energy is approximately 3% over 500 μs, and the current changes less than 0.2% in that time, so the absence of sources does not affect the conclusions here. Except where specified otherwise, we use a two-temperature model (model #4 in appendix).
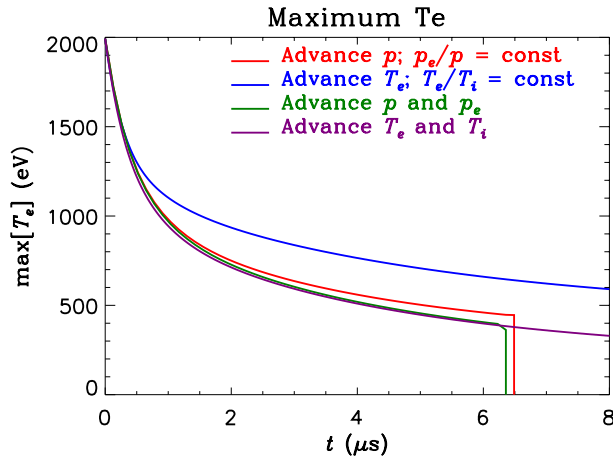
Figure 2. The maximum value of T_e in the initial few μs of the 2D simulation, as calculated using several different temperature evolution models. The four models here correspond respectively to the four models in appendix.

M3D-C1 uses an unstructured mesh of triangular reduced quintic finite elements in the poloidal plane [24]. Cubic Hermite elements are used in the toroidal direction. For the results presented here, the triangular elements are roughly uniform in size, each about 2.5 cm wide, and 32 toroidal planes have been used. Because the Hermite elements have two degrees of freedom per node, 32 equally spaced toroidal planes corresponds roughly to the same toroidal resolution as 32 toroidal Fourier modes. A simulation with eight toroidal planes shows the same qualitative behavior as the 32-plane case.

Neutral argon gas is introduced uniformly throughout the simulation domain as an initial condition, with density 10^{19} m^{-3} neutral atoms. This initial distribution of argon, of course, is not representative of how impurity gas is injected in an experiment. Our goal here is to explore the consequences of maximally assimilated impurities, rather than to validate against experimental results. To distinguish between axisymmetric and non-axisymmetric effects, we run both a non-axisymmetric (3D) and axisymmetric (2D) simulation with the same parameters.

In the simulation, the argon immediately begins to ionize. The electron temperature drops rapidly, primarily because of the rise in electron density. The drop in T_e, as calculated using the four different temperature evolution models described in appendix, is shown in figure 2. One salient feature of this figure is that the two models that evolve pressure rather than temperature become numerically unstable. This is a result of the fact that the pressure and density advance are separate in this implementation (the density is advanced before the pressure), and therefore parallel thermal conductivity $\vec{q}_e = -\kappa_\parallel^e \, \hat{b}\hat{b} \cdot \nabla(p_e/n_e)$, which is the dominant term in the pressure equation, is not treated fully implicitly. The other salient feature is that the assumption that T_e/T_i is constant leads to a markedly different solution. This is because the dominant forces acting on the electron temperature—namely, radiation and dilution by electrons shed by impurities and radiation—act only on the electron temperature, and therefore the physically correct result will have T_e/T_i decrease. The assumption that p_e/p is constant is more accurate here, because dilution dominates over radiation, and dilution does not affect either p_e or p.

Since the argon is uniformly distributed initially, the electron density rises most quickly near the magnetic axis, where the plasma is hottest and the ionization rate is largest. The radiation is also strongest near the magnetic axis, and therefore the thermal energy is dissipated most rapidly from that region. Even though the temperature drops most rapidly in the core, the resistivity rises most rapidly in the edge due to the $T_e^{-3/2}$ dependence of the resistivity. This causes the current channel to contract, which in turn causes the formation of skin currents, as can be seen in figure 3.

In the 3D simulation, these skin currents become unstable to non-axisymmetric modes. As can be seen from figure 4, the growth of these modes starts quite early, and no particular toroidal mode number has a clearly dominant growth rate, consistent with the peeling-like nature of the modes. In this case, the $n = 7$ mode grows to the largest amplitude first, but other intermediate-n modes such as $n = 12$ and $n = 14$ are competitive. As these modes grow, the magnetic fields outside of the current channel become stochastic, starting around $t \approx 60$ μs in this simulation. Eventually, the low-n perturbations grow to sufficient amplitude to stochasticize the magnetic field throughout the entire plasma. The Poincaré plots in figure 5 show the magnetic field structure just as the skin current instabilities reach a macroscopic size ($t = 64.9$ μs), and after these instabilities have destroyed all the magnetic surfaces in the plasma ($t = 130$ μs). These current sheet instabilities are similar to those reported by Ebrahimi in simulations of coaxial helicity injection in NSTX [25, 26].

The evolution of the total thermal energy and the thermal energy of the electrons is plotted in figure 6. The rapid initial drop in thermal energy is primarily due to line radiation from the impurities. (Note that the addition of electrons from ionizing impurities reduces the electron temperature, but does not reduce the thermal energy.) Subsequently, the total energy continues to decrease on $\sim$1 ms timescales due to conductive losses, but the electron thermal energy actually increases slightly as the electrons slowly thermalize with the ions. In 2D, this slow thermal quench continues until the thermal energy is dissipated—evidently, in this case, radiation from the argon is not enough to cause a complete, fast thermal quench without the associated MHD instabilities. In 3D, the global stochastization of the magnetic field due to the instability of the skin current leads to a rapid thermal quench, starting at about $t = 100$ μs. This thermal quench is primarily due to parallel thermal transport along stochastic field lines, although a burst of radiation is also seen at this time due to line radiation from the cooling impurities.

The rapid thermal quench after the field stochasticizes leads to a rapid increase in the rate of the current quench, as can be seen in figure 6. This is simply due to the increased resistivity of the cooled plasma, and is accompanied by an increase in ohmic heating in the core. After the skin currents
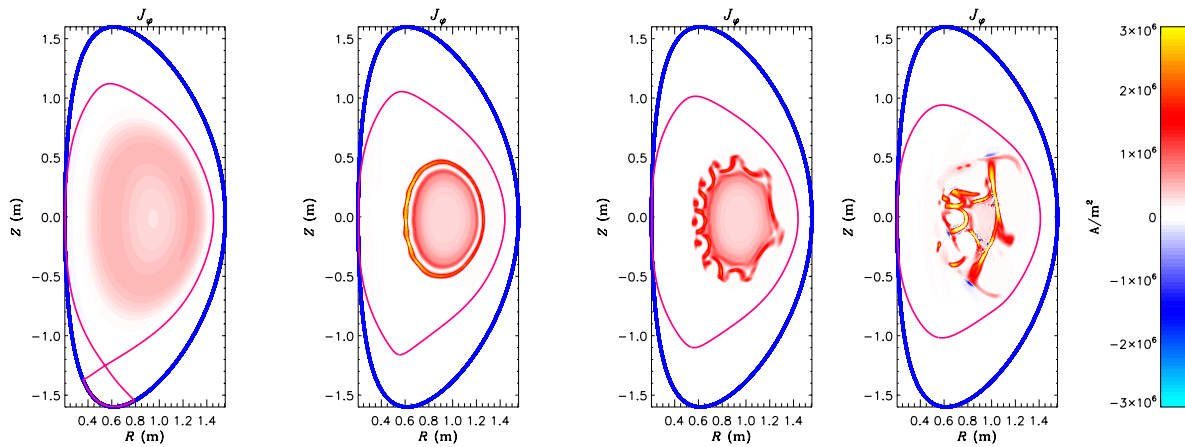
Figure 3. The toroidal current density in the 3D simulation at $t = 0, 51.9, 64.9$, and 116.8 μs after the introduction of neutral argon. The magenta curve indicates the last closed flux surface, and the blue curve indicates the computational domain boundary.
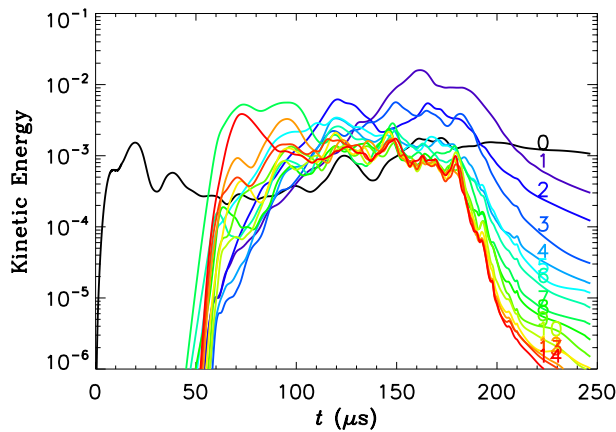

Figure 4. The kinetic energy in the $n = 0$–14 Fourier components of the 3D simulation.

have been destroyed by the instabilities, the magnetic geometry returns to axisymmetry. In this simulation, magnetic surfaces begin to form near the magnetic axis by $t \approx 190$ μs, and the magnetic surfaces are fully recovered throughout the plasma by $t \approx 230$ μs.

Large, spatially localized spikes in the maximum value of the parallel electric field $\vec{E}_{\parallel}$ are observed during the stochastic phase of the 3D simulation. Before this phase, $\vec{E}_{\parallel}$ remains axisymmetric with a peak of roughly 300 V m^{-1} near the edge of the plasma. This is what is responsible for the formation of the skin currents, and the value is consistent with the dissipation of the 0.34 Wb of poloidal flux over a period of roughly 250 μs. In the stochastic phase, the $\vec{E}_{\parallel}$ is non-axisymmetric and briefly exhibits local peaks at over 1500 V m^{-1}. After the stochastic phase, when the magnetic surfaces have largely healed, the maximum value of $\vec{E}_{\parallel}$ returns to roughly 300 V m^{-1}, now peaked at the magnetic axis.

Even in the axisymmetric phase, the value of $\vec{E}_{\parallel}$ significantly exceeds the critical electric field for the formation of runaway electrons [27], which is roughly 0.1 V m^{-1} here. In

this particular case, a significant runaway electron current might not be expected because the *e*-folding time for formation of runaways by the avalanche process [28] is comparable to the current quench time, and also because the stochastic fields during the period where $\vec{E}_{\parallel}$ is large would be expected to deconfine runaway electrons effectively.

We note that there is a small current spike in both the 2D and 3D simulations during the first $\sim$10 μs, at which time the core electron temperature is rapidly decreasing due to dilution by electrons from impurity ions. This current spike is clearly associated with a brief drop in the internal inductance of the plasma, suggesting that the spike is a result of redistribution of plasma current together with conservation of flux at the simulation boundary. However, no current spike is observed during the thermal quench caused by the stochastization of the magnetic field in the 3D simulation.

5. Discussion

We have described extended-MHD models that include ionization, recombination, radiation, and transport of impurities, and demonstrated the implementation of these models in M3D-C1. These models include the evolution of individual impurity charge states. Models using a single temperature equation conserve total energy—in the sense that all sources and sinks of energy are physical processes included in the model—but do not conserve electron energy. Models using two temperature equations conserve both total energy and electron energy independently.

For models with a single temperature equation, the assumption that T_e/T_i is constant is less accurate than the assumption that p_e/p is constant in cases where the ionization rate is fast compared to the electron–ion temperature equilibration rate, since ionization primarily cools electrons through dilution, which causes T_e to drop as p and p_e remain constant. This is an important consideration for simulations of disruption mitigation through massive gas injection or pellet injection, in which impurities are rapidly ionized by a hot plasma
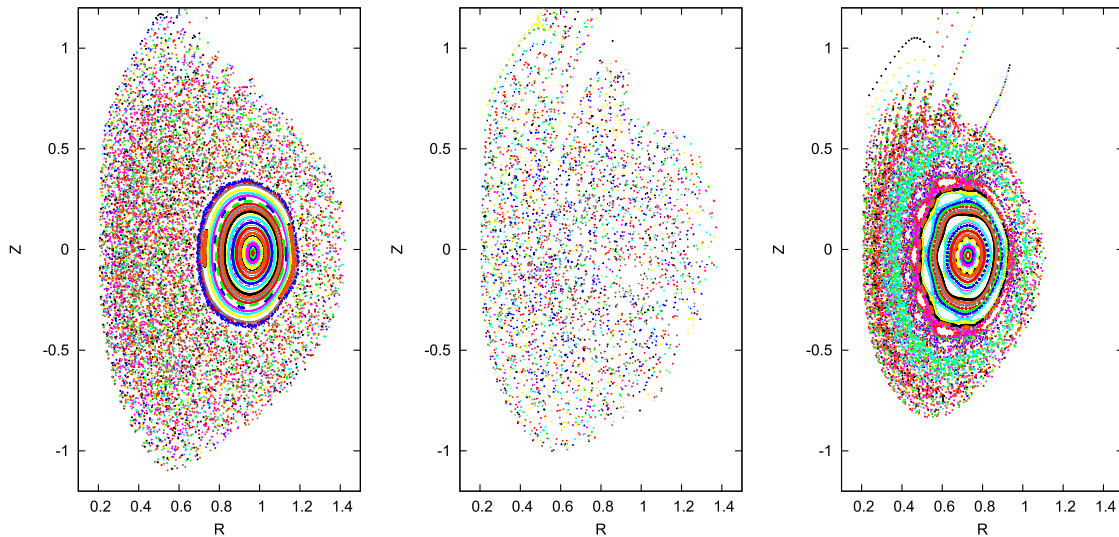
Figure 5. Poincaré plots showing the magnetic field structure at $t = 64.9\ \mu$s, $130\ \mu$s, and $221\ \mu$s.

where the collision rate (and hence electron–ion' temperature equilibration rate) is slow. In the post-thermal quench phase, where the plasma is cold ($\lesssim 10$ eV), the assumption of constant T_e/T_i may be significantly more accurate, although processes leading to disparate ion and electron confinement times such as open magnetic field lines may affect this.

It appears that 'coronal equilibrium' models, where it is assumed that the charge state densities are always in local thermal equilibrium (which we do not assume here), would be less accurate in modeling events such as the one considered in section 4.2. Indeed, in this case the electron density evolves due to ionization on timescales on the order of $100\ \mu$s, with sharp changes occurring during the initial ionization phase and, in the 3D simulation, during the thermal quench caused by stochastization. Furthermore, the individual charge state distribution evolves on an even longer timescale, taking several milliseconds to equilibrate at typical plasma parameters in simulations of trace impurities. Fortunately, while it is more burdensome to evolve the density of each charge state individually, it is not overly so; in the 3D simulations, the impurity model (which includes the evolution of the charge state densities) takes less than 10% of the total runtime since these equations are not solved together implicitly with the more expensive MHD advance.

It was noted that in the simulation of the NSTX disruption, a current spike is observed during the initial axisymmetric cooling of the core, but is not observed during the subsequent thermal quench caused by the stochastization of the field. These results are apparently at odds with experimental data, which generally find that the current spike can be delayed from the initial thermal quench, and tends rather to be correlated with the end of the thermal quench or even later [29]. They also differ from previous findings of NIMROD simulations by Izzo [30, 31], who found current spikes associated with disruptive tearing modes in the presence of impurity radiation in C-MOD (although the scenario we consider differs significantly from those of Izzo, in which cooling appears to be dominantly in

the core due to a peaked impurity profile and also, in some cases, due to a 1/1 internal kink instability that flattened the temperature profile.) We also note that previous simulations of vertical displacement events with M3D-C1 have found that a spike in the plasma current can arise when the a displacing plasma touches the wall due to the loss of counter-IP currents induced on the surface of the plasma [19], similar to what has been proposed by [32]. It is not clear that this mechanism fully explains experimental results either, though, as it tends to vanish in the limit that the wall resistivity is small relative to the resistivity of the scrape-off layer, and also it would not be observed by a Rogowski coil outside of the resistive wall that carries the stabilizing eddy currents. Finally, we note that 2D simulations of disruptions in TFTR have found a current spike when hyper-resistivity is included [33]. This hyper-resistivity model is intended to account for fast reconnection that is not present in 2D simulations, and might not be properly treated in single-fluid resistive calculations [34]. It is hypothesized that this fast reconnection should rapidly flatten the current due to the condition that $\vec{B} \cdot \nabla(J_\parallel/B) = 0$ that is required for a force-free equilibrium in a stochastic field [35].

Fast stochastization of the magnetic field is indeed observed in the simulation presented here, despite the absence of hyper-resistivity; and yet, a current spike is not observed. In these simulations, rather than a rapid flattening of the current profile, we observe that the current density evolves turbulently through the stochastic phase, with significant localized perpendicular current densities balanced primarily by localized pressure gradients. These localized perpendicular currents relax the constraint that $\vec{B} \cdot \nabla(J_\parallel/B) = 0$, and apparently are responsible for preventing the rapid flattening of the current profile. The current profile relaxes toward the end of the thermal quench when the pressure forces become subdominant to viscous forces, but at this point the current quench is already well underway, and past the point where a current spike would be expected. The plasma self-inductance does decrease during this phase, but not faster than the current
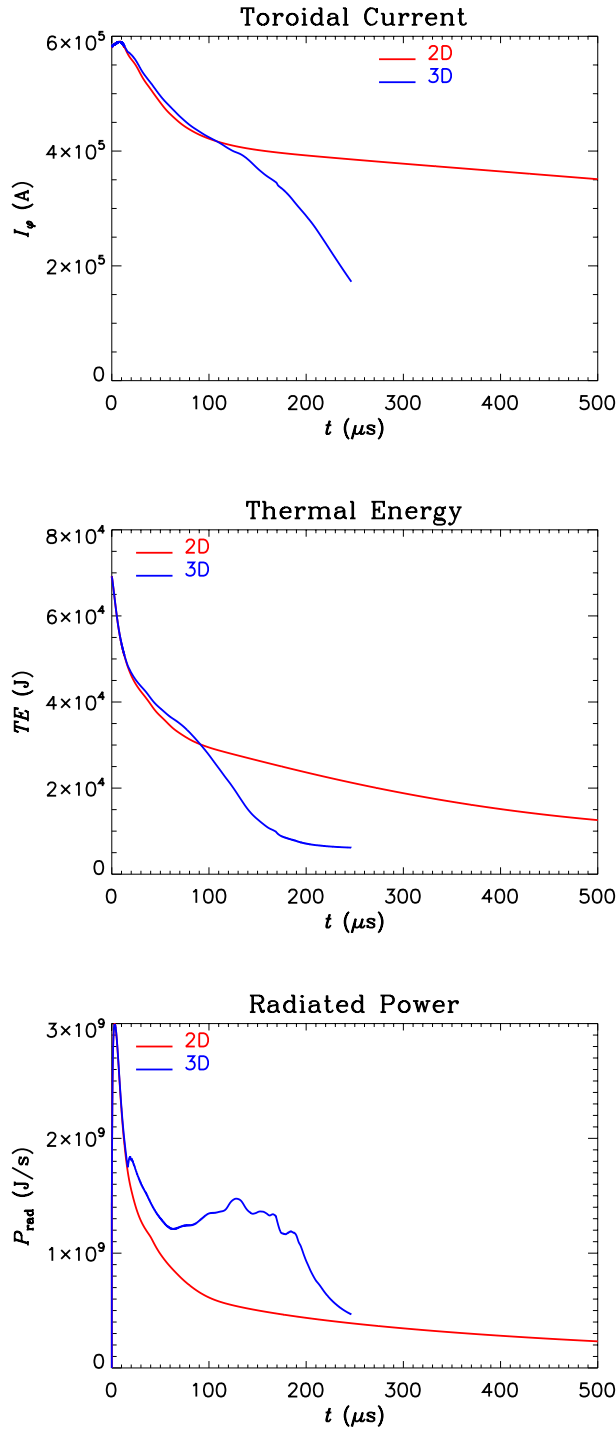
Toroidal Current

Thermal Energy

Radiated Power

Figure 6. The total toroidal current (top), thermal energy (center) and radiated power (bottom) in the 2D (red) and 3D (blue) simulations. In the plot of thermal energy, solid lines represent the total thermal energy, and dashed lines represent the thermal energy of the electrons.

decays through resistive dissipation. The fact that the current decay time is comparable to, or shorter than, the flattening time is a likely explanation for why no current spike is observed.

It is possible that this sequence of events would be changed by assuming a more realistic injection of impurities, in which the current quench phase might be delayed relative to the fast thermal quench due to less initial cooling from core ionization and radiation. In particular, our simulation differs from the scenario envisioned by Boozer in that we do not observe stochastization of the core first, due to overlapping of islands at rational surfaces, but rather we observe stochastization of the edge first, due to ideal instability of skin currents. Realistic models of impurity injection schemes will be considered in future work, and should help clarify the extent to which the injection strategy can control this sequence.

The evolution of the current profile has implications not just for the current spike, but also for MHD stability. Despite an impurity profile that is initially fully penetrated to the core, which causes cooling due to dilution and radiation to peak in the core, we find nevertheless that the current channel contracts rather than broadens. This is due to the strong dependence of the resistivity on the temperature that results in the resistivity being more sensitive to temperature changes in cool regions than in hot regions. The contraction of the current channel results in strong skin currents which become unstable and stochasticize the field, similar to what is seen in simulations of hot vertical displacement events [20], where the current contracts due to scraping off by the wall. Indeed, the internal inductance of the plasma is found to rise throughout this process. The fact that the current channel contracts even for maximally mixed impurities demonstrates the essential difficulty of cooling the plasma while avoiding a fast thermal quench due to stochastization through impurity injection. It may be possible to maintain closed surfaces at the edge of the plasma by highly localized cooling of the core (e.g. through the use of shell pellets [3]), but this has yet to be demonstrated.

We find that $\vec{E}_{\parallel}$ can exhibit large, spatially localized spikes due to the MHD instabilities caused by the contraction of the current channel. This may have implications for the the formation of runaway electrons, although a detailed model not presently available in M3D-C1 will be needed to quantify the formation and confinement of runaway electrons in an evolving, stochastic magnetic field. Work on implementing such a model in M3D-C1 is beginning and will be presented in future work. We do note that, in agreement with predictions, the strongest parallel electric fields prior to the thermal quench are observed on the surface of the plasma, and runaways formed there might be expected to be rapidly deconfined by any subsequent MHD activity. However, proper accounting of the generation of runaway electrons probably requires a self-consistent treatment of the electric field in the presence of runaways [36, 37].

Additional benchmarking between M3D-C1 and NIMROD is presently underway, and detailed comparisons of both 2D and 3D simulations will be presented in future work. These benchmark comparisons have already led to improvements in both codes. This progress underscores the value of having multiple codes that implement comparable models for the purpose of verification and validation.

Acknowledgments

Appendix. Temperature models in M3D-C1

The four models presently implemented in M3D-C1 for advancing the electron and ion temperatures are documented here.

A.1. Model 1: single pressure equation

This model includes a single pressure equation, which is the sum of the pressure equations for all charged species (neutral particles are assumed to have negligible thermal energy density and are excluded):

$$\frac{\partial p}{\partial t} + \vec{v} \cdot \nabla p + \Gamma p \nabla \cdot \vec{v} = (\Gamma - 1)$$
$$\times \left[\eta J^2 - \nabla \cdot \vec{q} + Q - \Pi : \nabla \vec{v} + \frac{1}{2} \varpi v^2 \right]. \tag{A.1}$$

Here, Π, Q, and $\vec{q}$ are the sum over all charged species. The electron pressure is assumed to be a fixed fraction of the total pressure ($p_e/p = \alpha_p$). The electron and ion temperatures are then determined by

$$T_e = p_e/n_e \tag{A.2}$$

$$T_i = \frac{(1 - \alpha_p) p}{n_i + \sum_{j=1}^{Z} n_Z^{(j)}}. \tag{A.3}$$

This model conserves total energy, but does not conserve electron energy independently.

A.2. Model 2: single temperature equation

This model includes a single temperature equation, which is the sum of the temperature equations for all charged species. The equation is written in terms of the electron temperature T_e, and assumes that the ratio of the ion to electron temperature is constant and uniform ($T_i/T_e = \alpha_T$).

$$N \left[\frac{\partial T_e}{\partial t} + \vec{v} \cdot \nabla T_e + (\Gamma - 1) T_e \nabla \cdot \vec{v} \right] + \Sigma T_e$$
$$= (\Gamma - 1) \left[\eta J^2 - \nabla \cdot \vec{q} + Q - \Pi : \nabla \vec{v} + \frac{1}{2} \varpi v^2 \right] \tag{A.4}$$

where

$$N = n_e + \alpha_T \left(n_i + \sum_{j=1}^{Z} n_Z^{(j)} \right) \tag{A.5}$$

$$\Sigma = \sigma_e + \alpha_T \left(\sigma_i + \sum_{j=1}^{Z} \sigma_Z^{(j)} \right). \tag{A.6}$$

This model is similar to model #1, but differs in that the ratio of the electron temperature to ion temperature is fixed rather than the ratio of the electron pressure to total pressure. As with model #1, this model conserves total energy but does not conserve electron energy independently.

By expressing the equations in terms of the temperature rather than the pressure, these equations simplify the calculation of $\vec{q}$, which is often the dominant term.

A.3. Model 3: total pressure and electron pressure equations

This model includes two pressure equations: equation (A.1) for the total pressure, and a separate equation for the electron pressure:

$$\frac{\partial p_e}{\partial t} + \vec{v} \cdot \nabla p_e + \Gamma p_e \nabla \cdot \vec{v} = (\Gamma - 1) \left(\eta J^2 - \nabla \cdot \vec{q}_e + Q_e - \Pi_e : \nabla \vec{v} \right). \tag{A.7}$$

This model conserves both total energy and electron energy independently.

A.4. Model 4: ion temperature and electron temperature equations

This model includes two temperature equations. The first is for the electron temperature individually

$$n_e \left[\frac{\partial T_e}{\partial t} + \vec{v} \cdot \nabla T_e + (\Gamma - 1) T_e \nabla \cdot \vec{v} \right] + \sigma_e T_e$$
$$= (\Gamma - 1) \left[\eta J^2 - \nabla \cdot \vec{q}_e + Q_e - \Pi_e : \nabla \vec{v} \right] \tag{A.8}$$

and the second is for the sum of all ion species (i.e. the main ions and all ionized impurities)

$$n_* \left[\frac{\partial T_i}{\partial t} + \vec{v} \cdot \nabla T_i + (\Gamma - 1) T_i \nabla \cdot \vec{v} \right] + \sigma_* T_i$$
$$= (\Gamma - 1) \left[-\nabla \cdot \vec{q}_* + Q_* - \Pi_* : \nabla \vec{v} + \frac{1}{2} \varpi v^2 \right] \tag{A.9}$$

where the '$*$' subscript indicates a sum over all ion species. Mathematically, this model is equivalent to model #3.

References

[1] Lehnen M. *et al* 2015 Disruptions in ITER and strategies for their control and mitigation *J. Nucl. Mater.* **463** 39

[2] Baylor L.R. *et al* 2009 Pellet fuelling, ELM pacing and disruption mitigation technology development for ITER *Nucl. Fusion* **49** 085013

[3] Hollmann E. *et al* 2010 Experiments in DIII-D toward achieving rapid shutdown with runaway electron suppression *Phys. Plasmas* **17** 056117

[4] Commaux N. *et al* 2010 Demonstration of rapid shutdown using large shattered deuterium pellet injection in DIII-D *Nucl. Fusion* **50** 112001

[5] Commaux N., Shiraki D., Baylor L., Hollmann E., Eidietis N., Lasnier C., Moyer R., Jernigan T., Meitner S. and Combs S. 2016 First demonstration of rapid shutdown using neon shattered pellet injection for thermal quench mitigation on DIII-D *Nucl. Fusion* **56** 046007

[6] Putvinski S., Barabaschi P., Fujisawa N., Putvinskaya N., Rosenbluth M. and Wesley J. 1997 Halo current, runaway electrons and disruption mitigation in ITER *Plasma Phys. Control. Fusion* **39** B157

[7] Fable E., Pautasso G., Lehnen M., Dux R., Bernert M., Mlynek A. and The ASDEX Upgrade Team 2016 Transport simulations of the pre-thermal-quench phase in ASDEX upgrade massive gas injection experiments *Nucl. Fusion* **56** 026012

[8] Pestchanyia S., Koslowski R., Reuxb C., Lehnen M. and JET EFDA Contributors 2015 Simulation of MGI efficiency for plasma energy conversion into Ar radiation in JET and implications for ITER *Fusion Eng. Des.* **96–7** 685

[9] Pautasso G., Zhang Y., Reiter B., Giannone O.G.L., Herrmann A., Kardaun K.K.O., Lukash V. and Maraschek M. 2011 Contribution of ASDEX upgrade to disruption studies for ITER *Nucl. Fusion* **51** 103009

[10] Jardin S., Schimdt G., Fredrickson E., Hill K., Hyun J., Merrill B. and Sayer R. 2000 A fast shutdown technique for large tokamaks *Nucl. Fusion* **40** 923

[11] Izzo V.A., Whyte D.G., Granetz R.S., Parks P.B., Hollmann E.M., Lao L.L. and Wesley J.C. 2008 Magnetohydrodynamic simulations of massive gas injection into alcator C-Mod and DIII-D plasmas *Phys. Plasmas* **15** 056109

[12] Whyte D.G. *et al* 1997 Energy balance, radiation and stability during rapid plasma termination via impurity pellet injections on DIII-D *Technical Report* GA-A22639 General Atomics

[13] Izzo V.A. 2013 Impurity mixing and radiation asymmetry in massive gas injection simulations of DIII-D *Phys. Plasmas* **20** 056107

[14] Izzo V.A., Parks P.B., Eidietis N.W., Shiraki D., Hollmann E.M., Commaux N., Granetz R.S., Humphreys D.A., Lasnier C.J. and Moyer R.A. 2015 The role of MHD in 3D aspects of massive gas injection *Nucl. Fusion* **55** 073032

[15] Fil A. *et al* 2015 Three-dimensional non-linear magnetohydrodynamic modeling of massive gas injection triggered disruptions in JET *Phys. Plasmas* **22** 062509

[16] Nardon E., Fil A., Hoelzl M., Huijsmans G. and JET contributors 2017 Progress in understanding disruptions triggered by massive gas injection via 3D non-linear MHD modelling with JOREK *Plasma Phys. Control. Fusion* **59** 014006

[17] Izzo V. 2017 The effect of pre-existing islands on disruption mitigation in MHD simulations of DIII-D *Phys. Plasmas* **24** 056102

[18] Jardin S.C., Ferraro N., Luo X., Chen J., Breslau J., Jansen K.E. and Shepard M.S. 2008 The M3D-C^1 approach to simulating 3D 2-fluid magnetohydrodynamics in magnetic fusion experiments *J. Phys.: Conf. Ser.* **125** 012044

[19] Ferraro N., Jardin S., Lao L., Shephard M. and Zhang F. 2016 Multi-region approach to free-boundary three-dimensional tokamak equilibria and resistive wall instabilities *Phys. Plasmas* **23** 056114

[20] Pfefferlé D., Ferraro N., Jardin S., Krebs I. and Bhattacharjee A. 2018 Modelling of NSTX hot vertical displacement events using M3D-C1 *Phys. Plasmas* **25** 056106

[21] Braginskii S.I. 1965 Transport processes in a plasma *Reviews of Plasma Physics* vol 1, ed M.A. Leontovich (New York: Consultants Bureau) pp 205–311

[22] Wesson J. 1987 *Tokamaks* (Oxford: Oxford University Press)

[23] Jardin S.C., Breslau J. and Ferraro N. 2007 A high-order implicit finite element method for integrating the two-fluid magnetohydrodynamic equations in two dimensions *J. Comput. Phys.* **226** 2146–74

[24] Jardin S.C. 2004 A triangular finite element with first-derivative continuity applied to fusion MHD applications *J. Comput. Phys.* **200** 133–52

[25] Ebrahimi F. 2016 *Phys. Plasmas* **23** 120705

[26] Ebrahimi F. 2017 *Phys. Plasmas* **24** 056119

[27] Connor J. and Hastie R. 1975 Relativistic limits on runaway electrons *Nucl. Fusion* **15** 415

[28] Rosenbluth M. and Putvinski S. 1997 Theory for avalanche of runaway electrons in tokamaks *Nucl. Fusion* **37** 1355

[29] Wesson J., Ward D. and Rosenbluth M. 1990 Negative voltage spike in tokamak disruptions *Nucl. Fusion* **30** 1011

[30] Izzo V. 2006 A numerical investigation of the effects of impurity penetration depth on disruption mitigation by massive high-pressure gas jet *Nucl. Fusion* **46** 541

[31] Izzo V. and Parks P. 2010 Comment on 'Plasma current spikes due to internal reconnection during tokamak disruptions' *Nucl. Fusion* **50** 058001

[32] Zakharov L.E. 2008 The theory of the kink mode during the vertical plasma disruption events in tokamaks *Phys. Plasmas* **15** 062507

[33] Merrill B., Jardin S., Ulrickson M. and Bell M. 1991 Dynamics and energy flow in a disrupting tokamak plasma *Fusion Eng. Des.* **15** 163

[34] Boozer A. 2017 Runaway electrons and ITER *Nucl. Fusion* **57** 056018

[35] Boozer A. 2018 Pivotal issues on relativistic electrons in ITER *Nucl. Fusion* **58** 036006

[36] Weng S.M., Sheng Z.M., He M.Q., Zhang J., Norreys P.A., Sherlock M. and Robinson A.P.L. 2008 Plasma currents and electron distribution functions under a DC electric field of arbitrary strength *Phys. Rev. Lett.* **100** 185001

[37] Breizman B. 2014 Marginal stability model for the decay of runaway electron current *Nucl. Fusion* **54** 072002